Materials Views
www.MaterialsViews.com

ADVANCED FUNCTIONAL MATERIALS
www.afm-journal.de

Structure and Energetics of Dislocations at Micro-Structured Complementary Interfaces Govern Adhesion

Congrui Jin, Anand Jagota, and Chung-Yuen Hui**

Highly enhanced adhesion can be achieved between surfaces patterned with complementary micro-channel structures. An elastic material, poly(dimethylsiloxane) (PDMS), is used to fabricate such surfaces by molding into a silicon master with micro-channel profiles patterned by photolithography. For each pair of complementary surfaces, dislocation defects are observed in the form of visible striations, where ridges fail to fully insert into the channels, and the rotational misalignment angle was found to be the key factor controlling the dislocation distribution and adhesion strength. Adhesion between complementary interfaces, as measured by energy release rate required to propagate an interfacial crack, can be enhanced by up to 30 times compared to a flat control depending on the misalignment angle. The ability to control the orientation and periodicity of dislocation patterns by changing misalignment angle makes this system eminently controllable. This system could be a useful experimental tool in assisting research on geometry-controlled adhesion, while providing a test-bed for stability theories of interacting dislocations and crack fronts.

1. Introduction

Adhesion selectivity via complementarity involves endowing surfaces with specific properties, such as texture, so that interaction between all except matching pairs is strongly attenuated. Various types of complementarity have been widely observed in nature, e.g., shape, charge, magnetic, and hydrogen-bonding.[1–12] The recent study by Singh et al.[13] provides a comprehensive list of references, both theoretical and experimental. Although the physical principles of complementarity in nature are quite well understood, the deliberate control of adhesion selectivity of material surfaces by complementarity has not been studied much as yet.[14] The possibility of adhesion selectivity between two flat surfaces with striped patterns of alternating positive and negative surface charges separated by an electrolyte has been analyzed by Bai et al. and Jin et al..[15,16] As for structural and shape complementarity, Vajpayee et al.[17] showed that highly selective adhesion can be achieved between complementary elastic surfaces patterned with ripples. Their results demonstrated that it is relatively simple to destroy adhesion between non-complementary surfaces. For example, rippled surfaces with different amplitudes or wavelengths do not adhere to each other. It is more difficult simultaneously to achieve selective adhesion and the basic question is whether and how the inevitably present small mismatches, either in the dimensions of the pattern or in alignment of the two sides of the interface, will be accommodated over length scales much larger than that of the repeating pattern. Singh et al.[13] investigated the adhesion enhancement between complementary surfaces with micro-channel structures in a rectangular-toothed pattern, and observed an interesting phenomenon: the appearance of defects in the form of visible striations.

In the present study, we examine the observed defect structures in detail. In particular, we establish their geometrical features to relate the local and global changes in the distribution and orientation of defect structures to factors influencing adhesion, such as misorientation and ridge/channel's geometrical parameters. We ask the questions: How do defect structures affect the interfacial adhesion? What is the enhancement due to complementarity and how is it attenuated by the defects? What is the nature of interfacial crack growth? How does the crack interact with the microstructure and with defects? To answer these questions quantitatively, we have carried out a series of well-controlled adhesion tests on complementary surfaces while progressively increasing the misalignment angle. It is hoped that such an approach will contribute to a better understanding of the effect of directional patterned heterogeneities on interfacial fracture energy between complementary surfaces, with potential implications for their use as adhesives, binders, coatings and sealants.

2. Experimental Methods

2.1. Sample Fabrication

To fabricate samples with micro-channel structures in a rectangular-toothed pattern on the surface, i.e., parallel channels with

C. Jin, Prof. C.-Y. Hui
Field of Theoretical and Applied Mechanics
Sibley School of Mechanical and Aerospace Engineering
Cornell University
Ithaca, NY 14850, USA
E-mail: ch45@cornell.edu

Prof. A. Jagota
Department of Chemical Engineering and Bioengineering Program,
Lehigh University
Bethlehem, PA 18015, USA
E-mail: anj6@lehigh.edu

DOI: 10.1002/adfm.201203337

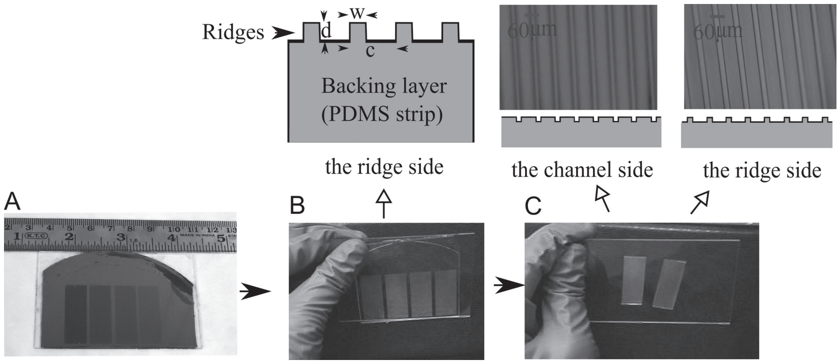

Figure 1. Illustration of sample fabrication. A typical piece of sample is 610 μm thick, 30 mm long and 10 mm wide. a) The etched silicon masters with parallel micro-channels on the surface patterned by photolithography. This silicon master contains four patterned areas. b) The cured PDMS layer was peeled off from the silicon master. This set of samples is called the ridge side. c) The channel side was obtained by a second molding and curing of PDMS on the first set of the samples. This figure also shows the optical micrographs of a pair of complementary surfaces.

a rectangular cross-section, we began by molding an elastomer, poly(dimethylsiloxane) (PDMS), into etched silicon masters with parallel micro-channels on the surface patterned by photolithography, as shown in **Figure 1**a. The channel width of the original masters, *w*, was fixed at 10 μm, the minimum center-to-center spacing or smallest period, *c*, was varied from 20 to 125 μm, and channel depth, *d*, was varied from 10 to 20 μm. This study is mainly focused on the case d = 10 μm. Liquid PDMS precursor (silicone elastomer base) was mixed with curing agent (Sylgard 184 Silicone Elastomer kit, Dow Corning) in weight ratio of 10:1. The liquid silicone mixture was then degassed under vacuum for 40 min before applying to the master and was cured at a temperature of 80°C for 120 min.

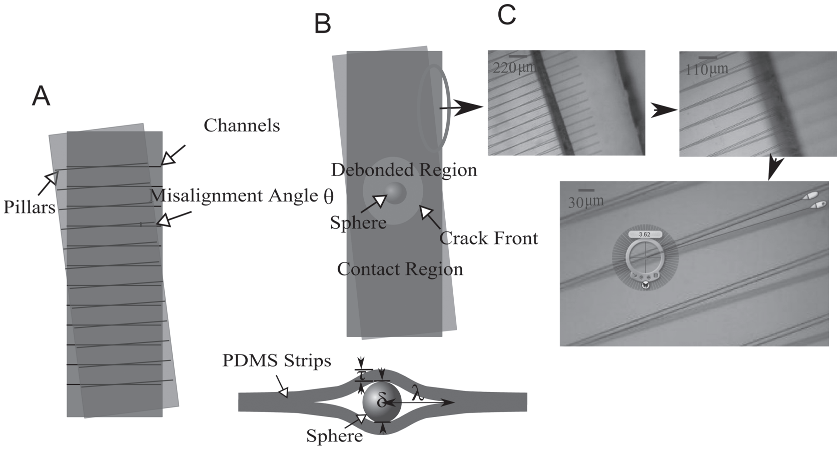

Figure 2. a) The rotational misalignment angle θ is the key factor in determining the relative orientation of the two complementary surfaces, and hence their adhesion strength. The interchannel spacing has been exaggerated in the diagram for visual clarity. b) Top view and cross-section schematic (not drawn to scale) of adhesion test by inserting a small glass sphere at the interface. c) Precise measurement of misalignment angle by analyzing the optical micrographs taken at the edges of the decohered PDMS strips. The value of misalignment angle was determined by making ten repeated measurements using the Screen Protractor (commercial software developed by Iconico, Inc.) with 0.01° resolution. The sample shown above has the same channel depth and width $d = w = 10$ μm, and $c = 110$ μm. Ten repeated measurements of the misalignment angle θ had a mean of 3.69° and a standard deviation of 0.52° in this case.

The cured PDMS layer, as shown in Figure 1b, was then peeled off the silicon master. A typical piece of sample is 610 μm thick, 30 mm long and 10 mm wide. This first PDMS sample is called the ridge side. The ridge side was coated by a monolayer of n-Hexadecyltrichlorosilane ($C_{16}H_{33}Cl_3Si$). A sample with a complementary surface profile, called the channel side, was obtained by a second molding and curing of PDMS on first set of the samples (i.e., the ridge side), as shown in Figure 1c, which also shows optical micrographs of a pair of complementary surfaces.

2.2. Adhesion Testing

The rotational misalignment angle θ, as defined in **Figure 2**a, is the key factor controlling the geometry and adhesion strength of the two complementary surfaces. We measured the adhesion of the complementary surfaces for different values of misalignment angle in the following manner, as shown in Figure 2b.

A small glass sphere of known diameter, δ, typically either 0.3 or 0.4 mm, is placed at the interface. We then press the two sheets against each other sufficiently, attempting to force ridges on one sheet to find and insert into the channels of the other. To simplify the analysis, both ends of the resulting sandwich structure are fixed on glass slides so that the expected debonding zone is freestanding, thereby ensuring that the two sheets are deflected equally in opposite directions. Immediately upon release of the pressing force, a crack propagates away from the sphere, since the sphere applies an opening displacement approximately equal to its diameter, and as a result, a debonded region forms between the two PDMS strips. Eventually the crack arrests at an equilibrium length, which results from a balance between energy release rate supplied by the debonded portion of the PDMS strip and the energy required to increase the crack area by a unit amount. The crack propagation was recorded by a Panasonic PV-GS400 3CCD Camcorder during the tests. Each video was stored together with a time stamp which allows each frame to be associated with a specific time. Using the dimensions of a folding ruler in the video images as spatial calibration, direct dimensional measurements could be made.

Since the solution of a circular interface crack between two flat elastic plates is known and consequently provides a baseline to compare against, control experiments were also carried out on unstructured, nominally flat samples of the same thickness. For structured samples, we waited for 2 h for the crack to achieve its equilibrium position; for flat

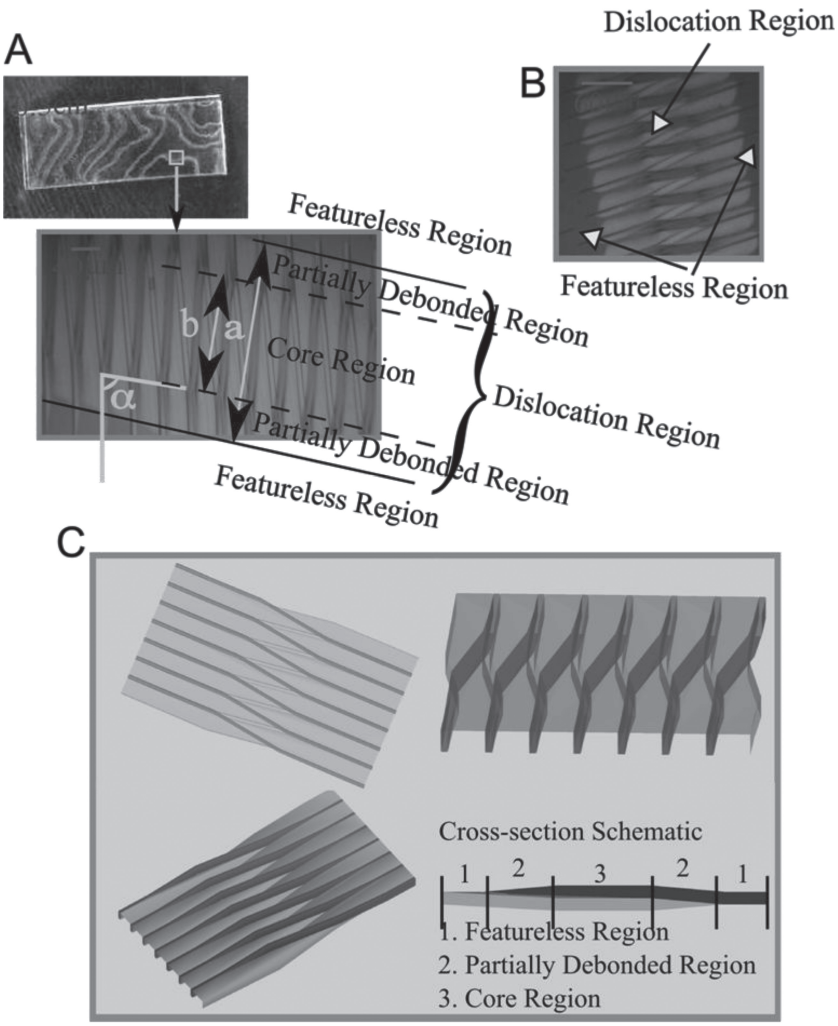

Figure 3. a,b) Photograph and optical micrographs of dislocation regions in complementary surfaces. The samples have the same channel depth and width, $d = w = 10$ μm, and a misalignment angle $\theta < 2°$. The interchannel spacing c: a) 40 μm and b) 30 μm. Clear, featureless regions are those where ridges have been inserted fully into channels. The striations are dislocation regions where ridges fail to fully insert into channels. The orientation of the dislocation region is described by the acute angle α. c) Schematic illustration of dislocation structures. A series of views from different angles show that the dislocation region where the ridges are completely pulled out and sheared sideways by a distance of c is clearly dilated.

control samples, a much longer time (up to 4 h) was needed. It is interesting to note that some samples (both flat and structured) appear to exhibit an equilibrium crack length after a relatively short time, although at much longer times, the crack length continues to increase.

Because the ridge structures have dimensions of order 10 μm, and the misorientation in the experiments is usually very small, adequate care must be taken to accurately measure the misalignment angle. In the experiments, directly after the properties (defined in the next section) of a pair of misaligned complementary surfaces had been measured, a thin wire was carefully inserted between the surfaces without changing the relative position between the two sheets, making the two PDMS strips decohere laterally from the corners. By analyzing the optical micrographs taken at the edges of the decohered strips, the misalignment angle θ was determined by making ten repeated measurements using the Screen Protractor with 0.01° resolution, as shown in Figure 2c.

3. Results and Discussion

3.1. Dislocation Structures

For any pair of complementary surfaces, when we try to insert ridges into their complementary channels, even with great care taken to align the two PDMS strips, we invariably observe defects in the form of visible striations tens to hundreds of microns in width where ridge/channel combinations are not fully inserted. The striations are visible because of light scattering from interfacial regions in partial contact. Away from the striation are featureless regions where the ridges are perfectly inserted into the channels, as shown in **Figure 3**. For additional examples, see Figure S1 in the Supporting Information. In the visible striations, ridges are first partially debonded from their corresponding channels, and then extracted from their channels and shifted over by one period in the core region, and finally partially inserted into a neighboring channel. The striations can thus be viewed as "screw dislocations" that carry a Burgers vector $\vec{\beta}$ with its magnitude equal to the value of interchannel spacing c, i.e., $|\vec{\beta}| = c$. (The dislocation is a pure screw dislocation only when the Burgers vector is perpendicular to the channel direction; otherwise, it is a mixture of screw and edge dislocations.) The dislocation region where the ridges are completely pulled out and sheared sideways by a distance of c is clearly dilated. Supporting Information Figure S1 also shows that these dislocation regions become wider as the inter-channel spacing, c, increases, and as a result, some intricate dislocation patterns, such as closed loops, as shown Supporting Information Figure S2, are only observed in the samples with small interchannel spacings ($c < 60$ μm) because of the limited sample size (30 mm × 10 mm).

Some of the salient properties of dislocation structures will be explored in the next section: the local geometric properties, such as the widths of the dislocation region and the core region (i.e. a and b, respectively, as defined in Figure 3a), and the dilation of the core region; and a series of general properties, such as the distance between dislocation regions, the orientation of the dislocation regions (i.e., the acute angle α between the tangent to the dislocation curve and the channel direction, as defined in Figure 3a).

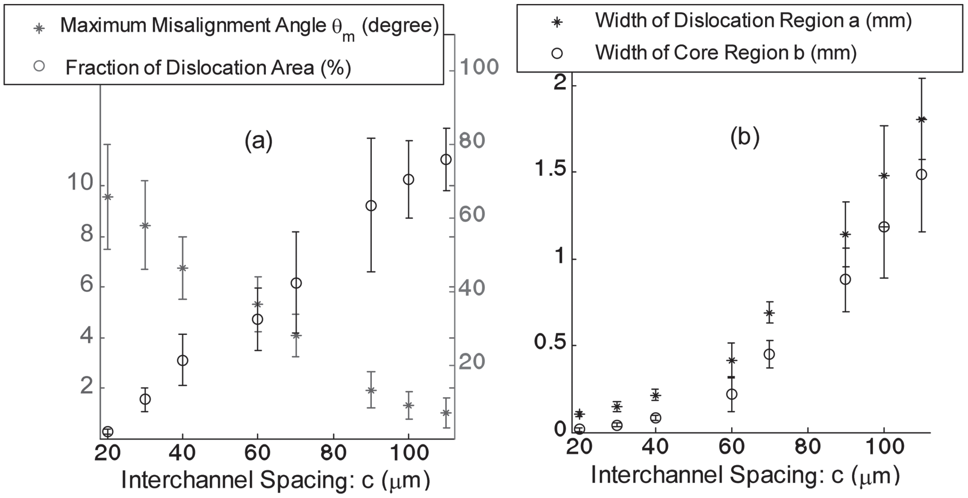

Figure 4. a) Maximum misalignment angle θ_m and the fraction of dislocation area in one sample as a function of interchannel spacing c when $\theta < 2°$. b) Widths of the dislocation region a and core region b as a function of interchannel spacing c when $\theta < 2°$. Error bars represent standard deviation from *7* different samples. All the samples have the same channel depth and width, $d = w = 10$ μm.

3.2. Rotational Misalignment

Rotational misalignment is one of the principal reasons that the dislocation defects occur. The rotational misalignment angle θ is defined in Figure 2a. The adhesion reduction due to a small angular misalignment is surprisingly large. Here we define θ_m as the maximum angle θ allowed between two PDMS strips when featureless regions can still be observed, and thus when $\theta > \theta_m$ there exists negligible adhesion between the two sheets. We found that $\theta_m < 10°$ for all the samples tested, and θ_m decreases with increasing interchannel spacing c, as shown in **Figure 4**a.

3.2.1. Case 1: Nearly perfect alignment when θ < 2°

When $\theta < 2°$, only a few dislocation regions are found. Since they show no regular pattern, no generalizations can be made about the possible causes for the defect. It could be a mixture of local mismatch, relative shear, misorientation, non-uniformity in pressing force and/or material properties, wherein there is no single dominant factor. Nonetheless, some general trends have been observed. The width of the dislocation region a, the width of the core region b, and the fraction of dislocation area in one sample, as a function of interchannel spacing c (when $\theta < 2°$), are presented in Figure 4. It shows that the fraction of area covered by defects in one sample is approximately proportional to c, consistent with our previous study.[13] It also shows that the widths of the dislocation and its core regions both increase with increasing inter-channel spacing, c.

The surface profile of the resulting sandwich structure, measured using an interferometric optical profilometer (ZeGage. Zemetrics, Inc), confirmed the dilation of the core regions. A typical surface profile is shown in Supporting Information Figure S3. The region on the surface right above a dislocation is usually 0.4 μm to 0.8 μm higher than that above a featureless region. As discussed in the next section, the local geometric properties of the dislocation region, such as the widths of the dislocation and core regions, and the dilation of the core region, do not depend on the misalignment angle. On the other hand, the fraction area covered by defects will change as the misalignment angle is increased, as shown in Figure 4a.

3.2.2. Case 2: Moderate misalignment when $2° < \theta < \theta_m$

As we gradually increase the misalignment angle θ to about 2.5°, the rotational misorientation plays a dominant role in the formation of dislocation structures, and as a result, the initially almost random distribution of dislocation regions resolves into a periodic pattern, which is the most striking and reproducible observation of the experiments, as shown in **Figure 5**a. The dislocation regions are fairly uniformly distributed over the entire interface, including the edges and corners, as shown in Supporting Information Figure S4. The experimental values for angle α usually fall within the range of $80° < \alpha < 90°$, i.e., in most cases, the Burgers vector is perpendicular (or nearly so) to the channel direction. The experimental results also show that the local geometric properties of the dislocation region, such as the widths of the dislocation region and the core region, and the dilation of the core region, depend only on the characteristic lengths of the rectangular-toothed channel pattern, i.e., the values of *w, d*, and *c,* and not on the misalignment angle, which means that the angular misalignment affects only the dislocation density, not its internal structure.

For a fixed misaligment angle, we observed spatial variation in dislocation density caused by non-uniformity in rotation, pressing force, material properties, and/or in-plane stretch, but the overall trend is clear and consistent that when the value of misalignment angle θ is increased, the density of the dislocation regions increases, and the area of the featureless region between the lines decreases. This trend is quantified in **Figure 6**, which plots the distance between dislocation regions, D, i.e., the pattern period, as a function of θ.

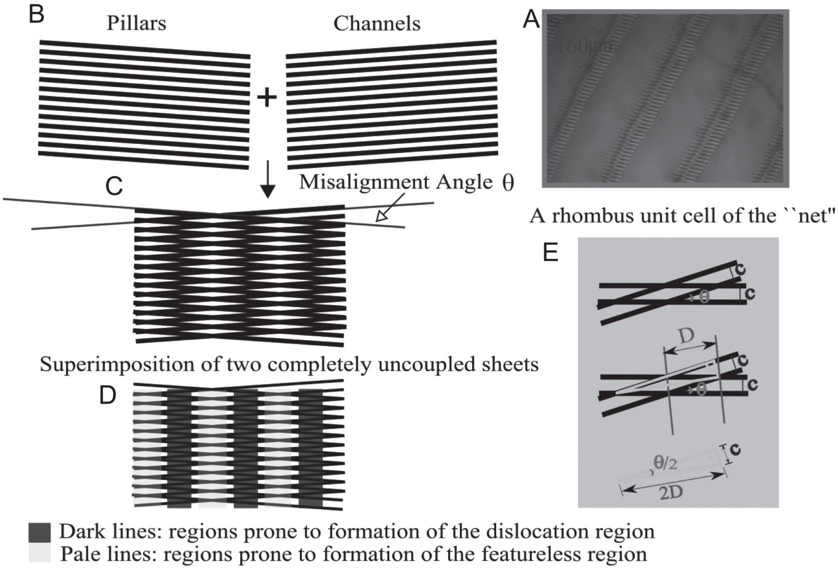

Figure 5. a) Optical micrograph of the periodic pattern of dislocation regions in misaligned complementary surfaces. The sample has the same channel depth and width, $d = w = 10$ μm, and the interchannel spacing $c = 30$ μm. The misalignment angle $\theta = 3.59°$. b–e): Schematic diagrams illustrating the formation of the observed periodic dislocation pattern in two rotationally misoriented complementary surfaces. A Moiré pattern is created by superimposing two sets of parallel and equidistant lines, one set rotated by a small angle with respect to the other.

The observed periodic dislocation pattern is actually a direct consequence of the superimposition of two moderately misoriented complementary surfaces. Figure 5b plots two identical sets of parallel and equidistant lines as a two dimensional simplification of a pair of complementary surfaces, one representing the channel side and the other representing the ridge side. When these two are superimposed with a small angular misorientation, a Moiré pattern[18–20] is obtained as shown in Figure 5c. As seen from a far distance, the Moiré pattern gives pale and dark periodic lines. As shown in Figure 5d, one can imagine that when the two samples are pressed against each other, the pale lines wherein ridges and channels are in close proximity to each other are prone to formation of the featureless regions, whereas the dark lines are prone to formation of the dislocation region.

A rhombus unit cell of the “net” is shown in Figure 5e, in which the misalignment angle is exaggerated for ease of illustration. Since the spacing between two pale lines is *D*, the longer diagonal of the rhombus is *2D*, which is the hypotenuse of the drawn right triangle. We thus obtain the following equation relating the spacing of the periodic dislocation pattern D to the interchannel spacing and the misalignment angle,

$$2D = c/\sin(\theta/2) \tag{1}$$

The *D*–θ relationship is plotted in Figure 6, which shows that the analytical result from Moiré analysis matches closely the experimental data for all the three types of samples. This result also demonstrates that local/global misalignment angle can be estimated through examination of the local/global Moiré pattern.

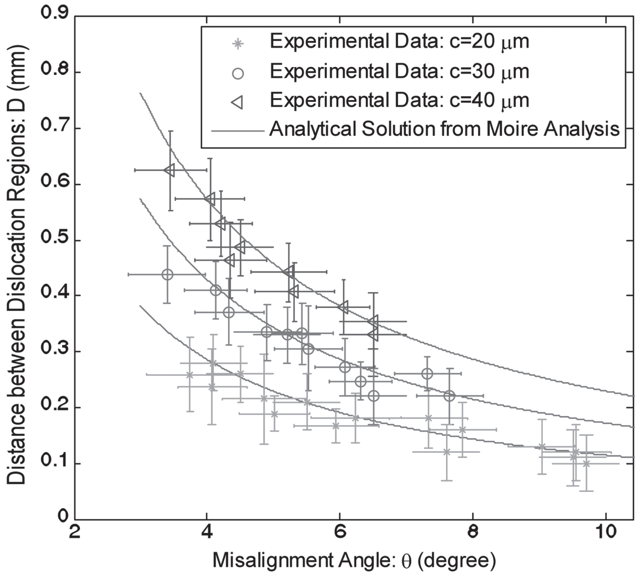

Figure 6. Distance between dislocation regions *D*, i.e., the pattern period, as a function of the misalignment angle θ. Error bars represent measurement errors, i.e., standard deviation from 10 repeated measurements within one sample. All the samples have the same channel depth and width, $d = w = 10$ μm, and the interchannel spacing c is varied from 20 μm to 40 μm. Some data were obtained from experiments performed on smaller samples (such as 8 mm × 10 mm in size) to reduce the effects of non-uniformity in rotation, pressing force, material properties, and/or in-plane stretch. These data are obtained from the samples in which the values for angle $>\alpha$ fall within the range of $75° < \alpha < 90°$, i.e., when the Burger’s vector are nearly perpendicular to the channel direction.

3.2.3. *Case 3: Severe misalignment when $\theta > \theta_m$*

Under severe misalignment condition $\theta > \theta_\mathrm{m}$, there exists negligible adhesion between the two sheets. The dislocation regions are so close-packed that no featureless region exists in between, and hence the entire sample scatters light. When θ is slightly larger than θ_m, however, the featureless region can be observed at first, but the defect structure is not stable, and as a result, the featureless regions in between start to shrink upon release of the pressing force, and gradually become spotty before they disappear altogether. Images from a video in Supporting Information Figure S5 represent details of two typical sequences.

3.3. Crack Propagation and Adhesion Strength between Complementary Surfaces

The two complementary strips are opened up by a displacement equal to the diameter of the sphere, δ, whose ratio to the thickness of the strip, τ, is always about 0.6 or less. Thus, the

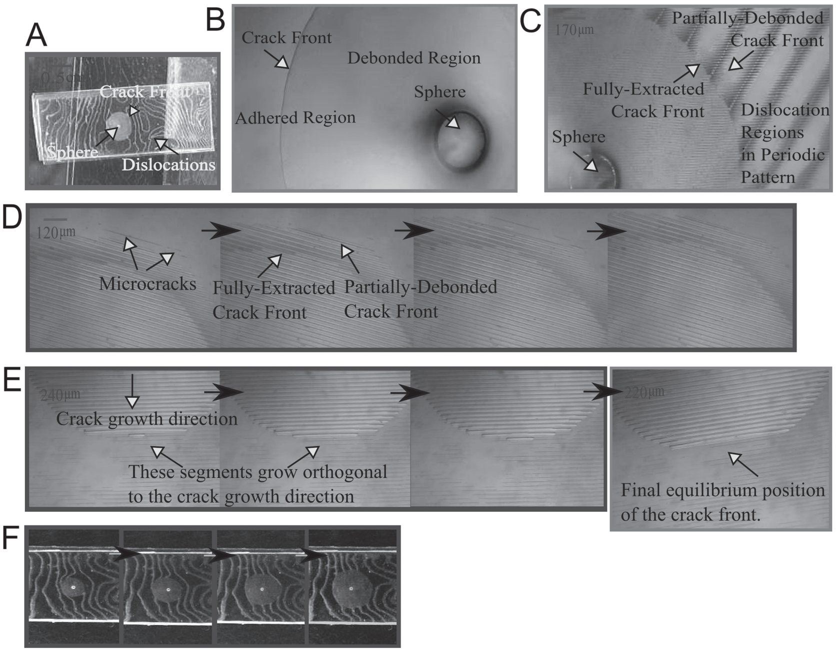

Figure 7. a) Photograph of a structured sample showing that the crack propagates away from the sphere and a debonded region forms. Also visible are a series of dislocations. b) Optical micrographs of the region behind and ahead of the crack front at the interface between two flat surfaces. c) A structured sample showing a crack advancing through a well-adhered region of the interface. As the misalignment angle increases, the random distribution of dislocation regions resolves into a periodic pattern. d,e) Images from a video representing details of typical sequences of the moving crack front, where nucleation, growth and coalescence of microcracks take place. d) These images are taken at time intervals of 12 s, while the first frame was acquired 20 s after release of the pressing force. e) These images are taken at time intervals of 8 s. Crack growth halted at a final crack length in the last frame. f) The influence of pre-existing dislocations on the shape of the debonded region can be substantial. The last frame shows the final equilibrium shape of the debonded region. All the samples shown above have d = w = 10 μm. The interchannel spacing: $c = 20$ μm in (a), (c), (d), $c = 30$ μm in (f), and $c = 40$ μm in (e). The misalignment angle: $\theta < 2°$ in (a), (d), (e), and (f), and $\theta = 4.65°$ in (c).

opening strips can be modeled as linearly elastic plates with Young's modulus E and Poisson's ratio ν. For flat samples, the equilibrium shapes of the debonded region are circular with radius λ, which is determined by setting the effective work of adhesion, W, equal to the energy release rate, G, which was shown to be:[21,22]

$$W = G = \frac{E\tau^3\delta^2}{6(1-\nu^2)\lambda^4}. \qquad (2)$$

For PDMS, the Poisson's ratio $\nu = 1/2$.

Figure 7 shows a photograph and microscopic images of the region near an advancing crack front. It can be seen that crack propagation on structured interfaces behaves quite differently from that on flat interfaces. For structured interfaces, there are two distinct fronts, one where the ridges have partially debonded from their complementary channels, and a second one behind which the ridges are fully extracted from their channels, consistent with observations from the previous study.[13] For structured samples, the shape of the debonded region is always close to circular, but never perfectly so, with or without the influence of dislocations. We therefore refer to its mean radius as crack length, still denoted by λ, such that $\pi\lambda^2$ is equal to area of the debonded region. The deviation from circularity, typically in the range of 3–15%, varies from sample to sample, and is not reproducible, even on the same sample.

3.3.1. Case 1: Nearly perfect alignment when $\theta < 2°$

The shape variability is mainly attributed to the stepwise nature of the crack propagation. The growth of the partially-debonded crack front is not continuous; rather, it is observed to proceed by the formation of new microcracks ahead of the moving partially-debonded crack front, which is followed by microcrack coalescence and further microcrack formation along the growth direction of the main crack. These microcracks consist of small sections of ridges pulled-out from their channels and are always initiated at the tip of the teeth in the rectangular-toothed channel pattern and then extend along the parallel channels, as shown in Figures 7d,e. Presumably, local stress concentrations determine which tooth segments crack first. This irregular ``staircase" pattern of crack growth is also evident with the fully-extracted crack front, which immediately follows the partially-debonded front. This discontinuous nature of the interfacial crack growth process is not surprising. The crack front is trapped as it tries to kink in a direction perpendicular to its original path. It is well known that the energy release rate at the tip of a kinked crack can be significantly less than its value prior to kinking. For example, the energy release rate at the tip of kinked crack, where the kink angle is 90° from the initial crack plane, is only 25% of the energy release rate that would exist if the crack had advanced straight ahead.[13,23] Therefore, even in dislocation-free zones, the directionally patterned heterogeneous interface does not simply unzip in a continuous manner.

Experimental results show that dislocations caused by misorientation can be a source of strong local perturbations along the crack path. The direct interaction of a propagating crack with stationary dislocations can generate substantial crack front deflections, and as a result, the shape of the debonded region is strongly influenced by the distribution and orientation of the pre-existing dislocations, as shown in Supporting Information Figure S6.

We measured the equilibrium crack length, λ, and then converted it into effective interfacial adhesion energy, W, using Equation (2). **Figure 8** plots the effective interfacial adhesion energy normalized by its value for a flat control. For each set of samples, we made 10 repeated tests. The first striking observation is that one can achieve a significant enhancement of adhesion, up to a factor of 30, over the flat control. Second, it is noticeable that, due to the influence of randomly distributed dislocations, despite the general trend that the equilibrium

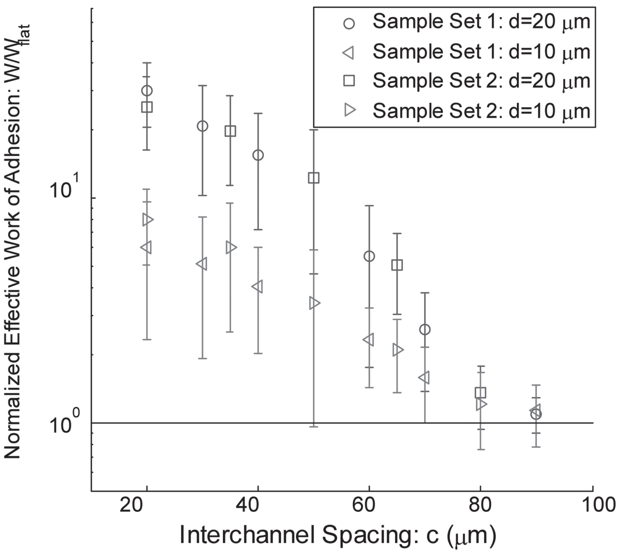

Figure 8. Normalized effective work of adhesion for different values of interchannel spacing, and two different channel depths (d = 10 and 20 μm). Error bars represent standard deviation from seven different samples. $W/W_{flat} = 1$ is represented by a horizontal line. The interchannel spacing c is varied from 20, 30, 40, 60, 70, to 90 μm in Sample Set 1; and from 20, 35, 50, 65, to 80 μm in Sample Set 2. All the samples shown above have $w = 10$ μm and $\theta < 2°$.

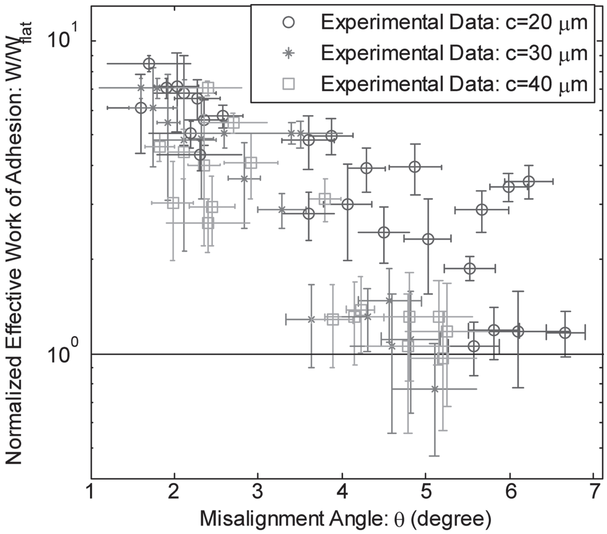

Figure 10. Normalized effective work of adhesion for different values of misalignment angle. Error bars represent measurement uncertainty, i.e., standard deviation from 7 repeated measurements. $W/W_{flat} = 1$ is represented by a horizontal line. All the samples have the same channel depth and width, $d = w = 10$ μm, and the interchannel spacing c is varied from 20 μm to 40 μm.

crack length increases with increasing c, the values of equilibrium crack length can differ significantly from sample to sample, and is not reproducible, even on the same sample. In a previous work,[13] we have analyzed that adhesion enhancement is mainly attributed to two mechanisms: crack trapping and frictional pull-out.

To understand the influence of dislocations on crack propagation, two typical crack-dislocation interaction sequences are illustrated in **Figure 9** and Supporting Information Figure S7. These images are taken at time intervals of 60 s, and the final equilibrium state of the crack front is shown on the right. It can be seen that the distance between the crack front and the dislocation continued to decrease until they coalesced. In the end, the crack did not cross the dislocation region, but rather travelled mainly along the orientation of the dislocation region, implying that the presence of dislocations alters the stress field near the crack front, and deflects the crack path from the preferred growth direction straight ahead.

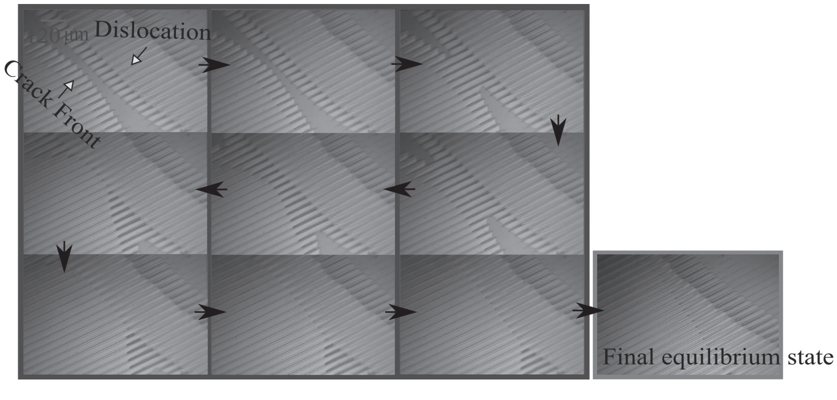

Figure 9. Images from a video representing a typical crack-dislocation interaction sequence. The sample has $d = w = 10$ μm, $c = 40$ μm, and $\theta < 2°$.

3.3.2. Case 2: Moderate misalignment when $2° < \theta < \theta_m$

As we gradually increase the misalignment angle, the random distribution of dislocation regions resolves into a periodic pattern, as shown in Figure 7c. Increasing the misalignment angle increases the dislocation density, which results in a lower adhesion strength, as shown in **Figure 10**, implying that the presence of the dislocation regions, while accommodating rotational mismatch between two complementary surfaces, is actually detrimental to adhesion. The concepts and results from the analysis of semi-coherent interfaces in crystalline solids in material science are closely connected to our research. We may apply the formula borrowed from the study of semi-coherent interfaces (including small-angle grain boundaries)[24–26] to analyze our experimental results at tens-of-micron scale. For example, the formula for the strain energy density as a function of misalignment angle given by Read and Shockley[25,26] can be applied to our case without much modification.

3.4. Relationship between Local Geometric Properties of Dislocation Structure and Interfacial Adhesion Strength

In the previous two sections, we discussed the local geometric features of the dislocation structure, e.g. the results shown in Figure 4b,

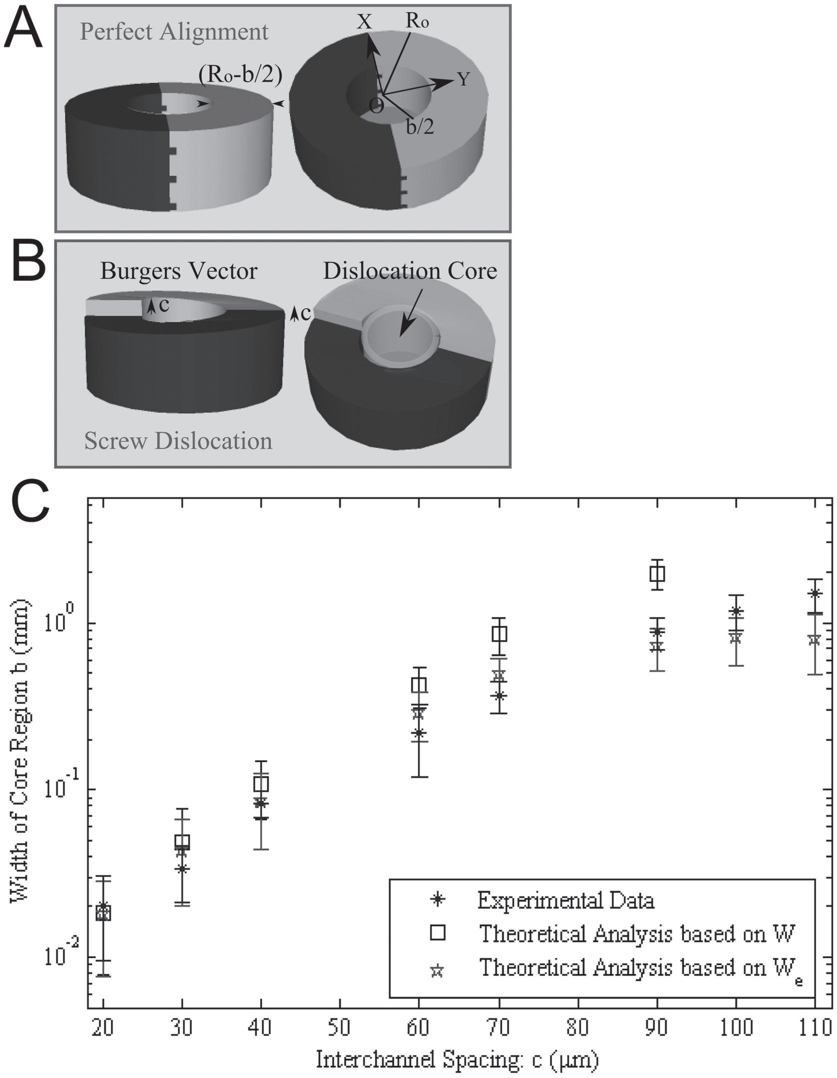

Figure 11. a) A pair of complementary surfaces in perfect alignment. Since the backing layers are very thick in comparison with the value of interchannel spacing c, they can be modeled as infinite elastic blocks. b) A defect structure viewed as a screw dislocation that carries a Burgers vector with magnitude of interchannel spacing c. c) The $b - c$ relationship based on Equation (3c) is compared against experimental data presented in Figure 4b.

and interfacial adhesion strength between complementary surfaces, e.g. the results shown in Figure 8 and Figure 10, respectively, and now we will examine whether there is actually a relationship between the two. Specifically, we investigate the relation between misorientation angle, the effective work of adhesion and interchannel spacing.

First, we note that, because of the disruption of the perfect periodicity around a screw dislocation, there is a strain energy per unit length, Ψ_s, in a region bounded by cylinders of radii $b/2$ and R_o ($R_o > b/2$), as shown in Figures 11a,b. Here b represents the diameter of the dislocation core and R_o a characteristic distance where the effect of the dislocation is small. The strain energy per unit length, $\Psi_s$depends quadratically on the magnitude of the Burgers vector c:[13,27]

$$\Psi_s = \frac{\mu c^2}{4\pi} \log \frac{2R_o}{b} \tag{3a}$$

where μ is the shear modulus of PDMS. Equation (3a) diverges as $b \to 0$, indicating failure of the continuum description near the core. As c increases, eventually its associated strain energy will exceed the adhesion energy of the interface and interfacial failure (unstable dislocation structure) will occur. An energy release rate balance between the work of separating the interface, $\Psi_\gamma = (2R_o - b)W$, where W is effective work of adhesion between complementary surfaces, and the strain energy from Equation (3a) (both per unit length) results in a relationship between b and W as follows:

$$\frac{d\Psi}{db} = 0 \ \rightarrow \ \frac{d\Psi_s}{db} - \frac{d\Psi_\gamma}{db} = 0 \tag{3b}$$

$$\rightarrow \quad b = \frac{\mu c^2}{4\pi W} \tag{3c}$$

Note that this result is independent of the choice of R_o. We compare the prediction of Equation (3c) with our experimental measured core widths. The theoretical core width b in Equation (3c) can be evaluated using the experimentally measured values of effective work of adhesion, W, in Figure 8 and using a typical value for shear modulus of PDMS, μ = 1.00 MPa,.[28] This comparison is shown in **Figure 11**c which shows that Equation (3c) overestimates the measured width of the dislocation core. This is because during the adhesion tests, all the elastic energy associated with these dislocations is released to assist crack growth. Thus the experimentally measured work of adhesion, W, which already includes a negative contribution from the defect structures, has a smaller value than that experienced by the growing dislocation core, W_e. Therefore, one should replace W in Equation (3c) by W_e. A reasonable value of W_e can be estimated using

$$W_e = \frac{\text{experimentally measured work of adhesion}}{1 - (\text{fraction area coveredby defects})\%}. \tag{4}$$

Recall that the fraction area covered by defects in typical samples with small misorientation is approximately proportional to c, as shown in Figure 4a. After this modification, the theoretical prediction given by (3c) matches the experimental measurements quite well, as shown in Figure 11c, establishing the conclusion that the size of the dislocation core is determined by balance of dislocation energy and interfacial adhesion.

The strain energy stored in the dislocation core has been neglected in our calculation above. It is possible to account for this energy by considering a smeared-out dislocation core instead of the ideal line dislocation where the strain energy diverges.[29,30] A more complete analysis given in SI shows that Equation (3c) remains correct even if we account for the elastic energy of the core. The energy release rate due to dilation of the core region is also addressed in SI, where we show that it may be neglected for our samples.

The results obtained through these experiments and analysis can aid the design of such adhesive surfaces. An important question is, how does θ_m (the maximum angle θ allowed between two PDMS strips when featureless regions can still be observed) depend on geometrical and materials parameters? This question can be answered based on Equation (1) and Equation (3), which provide the period of the dislocation pattern D and the width of dislocation core b, respectively. Assume that the periodic defect structure will not be stable when $D \approx nb$, where n is an integer somewhat greater than unity ($n \approx 5$). See Supporting Information Figure S5 and note that b represents the width of the dislocation core, not that of the dislocation region. We obtain the following relationship between θ_m and c using Equation (3c),

$$D \approx c/\theta_m \approx nb \rightarrow \theta_m \approx \frac{4\pi W_e}{n\mu c}. \tag{5}$$

which captures the experimental data provided by Figure 4a.

4. Conclusions

Following experimental indications that rotational misalignment angle is a key factor controlling dislocation pattern and adhesion strength between two micro-structured complementary surfaces, we have carried out a series of controlled adhesion tests on complementary surfaces while progressively increasing the misalignment angle.

It has been found that as the misalignment angle increases, the initially almost random distribution of dislocation regions resolves into a periodic pattern, i.e., the dislocation regions are fairly uniformly distributed over the entire interface, including the edges and corners, and as a result local/global misalignment angles can be estimated through examination of the local/global Moiré patterns. On the other hand, the local geometric properties of the dislocation region, such as the widths of the dislocation region and the core region, and the dilation of the core region, depend only on the characteristic lengths of the rectangular-toothed channel pattern, not on the misalignment angle, which means that the angular misalignment affects only the dislocation distribution, not its internal structure.

Experimental results show that direct interaction of a propagating crack with stationary or quasistationary dislocations can generate substantial crack front deflections, and as a result, the shape of the debonded region is strongly influenced by the distribution and orientation of the pre-existing dislocations. Adhesion between complementary interfaces, as measured by energy release rate required to propagate an interfacial crack, can be enhanced by up to 30 times compared to a flat control depending on the misalignment angle. The relationship between the local geometric features of the dislocation structure and interfacial adhesion strength between complementary surfaces can be obtained from an energy release rate balance analysis. The results obtained through these experiments and analysis form a knowledge base from which geometry-controlled adhesive surfaces can be designed. The dislocation patterning process is interesting both as a tool for fundamental and technological studies of defect structures and for its potential in applications in material science.

Supporting Information

Supporting Information is available from the Wiley Online Library or from the author.

Acknowledgements

This work was supported by the U.S. Department of Energy, Office of Basic Energy Science, Division of Material Sciences and Engineering under Award (DE-FG02-07ER46463). C.J. expresses her appreciation for the hospitality of A.J.'s group at Lehigh University when she was a visiting researcher there from December 2011 to November 2012. Mr. Ying Bai is thanked for helping to prepare experimental samples.

Received: November 14, 2012

---

[1] C. Chothia, J. Janin, *Nature* **1975**, *256*, 705.
[2] N. Bowden, S. Brittain, A. G. Evans, J. W. Hutchinson, G. M. Whitesides, *Nature* **1998**, *393*, 146.
[3] R. J. Jackman, S. T. Brittain, A. Adams, M. G. Prentiss, G. M. Whitesides, *Science* **1998**, *280*, 2089.
[4] W. Yang, R. L. Somerville, *Methods* **1999**, *19*, 322.
[5] P. W. K. Rothemund, *Proc. Natl. Acad. Sci. USA* **2000**, *97*, 984.
[6] E. Kangas, B. Tidor, *J. Phys. Chem. B* **2001**, *105*, 880.
[7] J. K. N. Mbindyo, B. D. Reiss, B. R. Martin, C. D. Keating, M. J. Natan, T. E. Mallouk, *Adv. Mater.* **2001**, *4*, 249.
[8] G. M. Whitesides, B. Grzybowski, *Science* **2002**, *295*, 2418.
[9] G. M. Whitesides, M. Boncheva, *Proc. Natl. Acad. Sci. USA* **2002**, *99*, 4769.
[10] V. N. Manoharan, M. T. Elsesser, D. J. Pine, *Science* **2003**, *301*, 483.
[11] M. Lamblet, E. Verneuil, T. Vilmin, A. Buguin, P. Silberzan, L. Leger, *Langmuir* **2007**, *23*, 6966.
[12] H. Shahsavan, B. Zhao, *Langmuir* **2011**, *27*, 7732.
[13] A. K. Singh, Y. Bai, N. Nadermann, A. Jagota, C.-Y. Hui, *Langmuir* **2012**, *28*, 4213.
[14] A. Jagota, C.-Y. Hui, *Mater. Sci. Eng., R* **2011**, *72*, 253.
[15] Y. Bai, C. Jin, A. Jagota, C.-Y. Hui, *J. Appl. Phys.* **2011**, *110*, 054902.
[16] C. Jin, Y. Bai, A. Jagota, C.-Y. Hui, *J. Appl. Phys.* **2011**, *110*, 054903.
[17] S. Vajpayee, K. Khare, S. Yang, C.-Y. Hui, A. Jagota, *Adv. Funct. Mater.* **2011**, *21*, 547.
[18] W. Bollmann, *Crystal defects and crystalline interfaces,* Springer-Verlag, Berlin **1970**.
[19] I. Amidror, *The Theory of the Moiré Phenomenon*, Kluwer Academic Publishers, Dordrecht, Netherlands **1999**.
[20] G. Oster, Y. Nishijima, *Sci. Am.* **1963**, *208*, 54.
[21] J. M. Sanchez, S. El-Mansy, B. Sun, T. Scherban, N. Fang, D. Pantuso, J. M. Sanchez, S. El-Mansy, B. Sun, T. Scherban, N. Fang, D. Pantuso, W. Ford, M. R. Elizalde, J. M. Martinez-Esnaola, J. Gil-Sevillano, M. Fuentes, J. Maiz, *Acta Mater.* **1999**, *47*, 4405.
[22] C. Jin, *Int. J. Solid. Struct.* **2008**, *45*, 6485.

[23] J. W. Hutchinson, Z. Suo, *Adv. Appl. Mech.* **1992**, *29*, 63.
[24] A. P. Sutton, R. W. Balluffi, *Interfaces in Crystalline Materials*, Oxford University Press, Oxford **1995**.
[25] W. T. Read, *Dislocations in Crystals*, McGraw-Hill, New York **1953**.
[26] W. T. Read, W. Shockley, *Phys. Rev.* **1950**, *78*, 275.
[27] J. P. Hirth, J. Lothe, *Theory of Dislocations*, McGraw-Hill, New York **1983**.
[28] W. L. Noderer, L. Shen, S. Vajpayee, N. J. Glassmaker, A. Jagota, C.-Y. Hui, *P. Roy. Soc., A* **2007**, *463*, 2631.
[29] W. Cai, A. Arsenlis, C. R. Weinberger, V. V. Bulatov, *J. Mech. Phys. Solids* **2006**, *54*, 561.
[30] J. Lothe, in *Elastic Strain Fields and Dislocation Mobility* (Eds: V. L. Indenbohm, J. Lothe), North-Holland, Amsterdam **1992**.